Experimental Eye Research 211 (2021) 108756

Contents lists available at ScienceDirect

Experimental Eye Research

journal homepage: www.elsevier.com/locate/yexer

In vivo imaging of the inner retinal layer structure in mice after eye-opening using visible-light optical coherence tomography

Lisa Beckmann [a], Zhen Cai [a], James Cole [b], David A. Miller [a], Mingna Liu [b], Marta Grannonico [b], Xian Zhang [a], Hyun Jung Ryu [a], Peter A. Netland [c], Xiaorong Liu [b,c,d,**], Hao F. Zhang [a,*]

[a] Department of Biomedical Engineering, Northwestern University, Evanston, IL, USA
[b] Department of Biology, University of Virginia, Charlottesville, VA, USA
[c] Department of Ophthalmology, University of Virginia, Charlottesville, VA, USA
[d] Department of Psychology, University of Virginia, Charlottesville, VA, USA

ARTICLE INFO

Keywords:
Optical coherence tomography
In vivo imaging
Retinal development

ABSTRACT

The growth of the mouse eye and retina after birth is a dynamic, highly regulated process. In this study, we applied visible-light optical coherence tomography (vis-OCT), a non-invasive imaging technique, to examine developing retinal layer structures after eye-opening. We introduced a resampled circumpapillary B-scan averaging technique to improve the inter-layer contrast, enabling retinal layer thickness measurements as early as postnatal day 13 (P13) – right after eye-opening. We confirmed vis-OCT measurements using *ex vivo* confocal microscopy of retinal sections at different ages. Our results demonstrate that vis-OCT can visualize the developmental murine retinal layer structure *in vivo*, which offers us new opportunities to better characterize the pathological alterations in mouse models of developmental eye diseases.

1. Introduction

After birth, the retina expands as the eye enlarges, a highly regulated developmental process (Sanes and Masland, 2015; Sernagor et al., 2001). Retinal ganglion cells (RGCs) are among the first to differentiate before birth, extending their axons to form the optic nerve (Cang et al., 2018; Cepko et al., 1996; Livesey and Cepko, 2001). The complex dendritic arbors of RGCs start to take shape with processes that diffusely ramify in the inner plexiform layer (IPL) and continue to refine after eye-opening (Liu et al., 2009; Tian and Copenhagen, 2003). Naturally occurring cell death or apoptosis also happens during the first two to three weeks after birth (Cepko et al., 1996; Livesey and Cepko, 2001). Approximately 50% of RGCs present at birth die within the first two postnatal weeks (Beros et al., 2018), and Müller cell degeneration also reaches a peak at postnatal days 8–11 (Young, 1984). In other words, even after birth, the inner retina goes through dramatic changes with neurogenesis, cell death, synaptic maturation, and refinement.

In developmental eye diseases, much remains to be investigated of how the inner retinal layers fail to develop with neuronal degeneration and death. For example, aniridia, a congenital eye disorder, develops varied retinal damages, such as foveal hypoplasia and optic nerve hypoplasia (Ginsberg et al., 1980; Kondo, 2018; McCulley et al., 2005). Moreover, about 50%–85% of aniridia patients develop an increased intraocular pressure (IOP) in late childhood or early adolescence, which results in further RGC death and subsequent vision loss as glaucoma progresses (Cole et al., 2021; Netland et al., 2011). *In vivo* examining and tracking of retinal structural changes with age will be needed to better understand how retinal neurons mature during normal development and how they degenerate with disease development and progression.

Some limitations to tracking developmental changes are the high resolution and sensitivity required for visualizing and quantifying the retinal layer structure *in vivo*. Near-infrared (NIR) optical coherence tomography (OCT) systems, operating at center wavelengths from 830 nm to 1330 nm, cannot satisfy this need because the axial resolution and contrast sensitivity are not sufficient to accurately measure minute inner retinal anatomical alterations (Shu et al., 2017). We and other groups developed visible light-OCT or vis-OCT, which provides 1.3-μm axial resolution in tissue, enabling the visualization of retinal sublayers in humans without using adaptive optics (Chong et al., 2018; Rubinoff et al., 2019; Zhang et al., 2019). We further established a novel imaging

* Corresponding author.
** Corresponding author. Department of Biology, University of Virginia, Charlottesville, VA, USA.
E-mail addresses: xl8n@virginia.edu (X. Liu), hfzhang@northwestern.edu (H.F. Zhang).

https://doi.org/10.1016/j.exer.2021.108756
Received 16 June 2021; Received in revised form 10 August 2021; Accepted 30 August 2021
Available online 4 September 2021

modality, vis-OCT fibergraphy (vis-OCTF), to visualize and quantify RGC axon bundles in adult mice (Miller et al., 2020), making tracking the postnatal development of the inner retinal layers *in vivo* possible.

However, blood absorbs visible light much more than near-infrared light (Smith et al., 2009). Therefore, vis-OCT imaging quality may be particularly affected by attenuation from the hyaloid vessels, which persist in young mice, precluding studies of normal development and pediatric eye diseases in mice. This study introduces a resampled circumpapillary B-scan averaging technique that improves inter-layer contrast in the retina, enabling reproducible retinal layer thickness measurements. We applied vis-OCT to image healthy wild-type mice from around the time of eye-opening (P13) to maturity (P60) and validated *in vivo* vis-OCT results by *ex vivo* confocal microscopy.

2. Materials and methods

2.1. Mice

We imaged wild-type C57BL/6 mice from P13 to P60. We separated these mice into four groups based on age: P13-16 (labeled as P14), P18-21 (labeled as P20), P28-31 (labeled as P30), and P50-60 (labeled as P60). These groups can be described as 1) right after eye-opening, 2) one week post-eye-opening, 3) two weeks post-eye-opening, and 4) mature adults. All animal protocols were approved by the Institutional Animal Care and Use Committees of Northwestern University and the University of Virginia.

2.2. Vis-OCT imaging

Prior to vis-OCT imaging, mice were anesthetized by intraperitoneal injection (10 mL/kg body weight) of a ketamine/xylazine cocktail (ketamine: 11.45 mg/mL; xylazine: 1.7 mg/mL, in saline). Tropicamide (1%; Henry Schein Animal Health) dilated the pupils of the mice after they had been anesthetized and prior to vis-OCT imaging. The mice were then immobilized on a homemade animal holder for vis-OCT imaging (Chen et al., 2016). An infrared heat lamp maintained each mouse's body temperature during imaging. Artificial tear drops were applied every few minutes to prevent corneal dehydration.

The details of the experimental vis-OCT system have been previously reported (Chen et al., 2016). The power incident on the cornea was 1 mW, and an A-line rate of 25 kHz was used. We acquired a rectangular OCT angiography (OCTA) dataset (400 A-lines × 512 B-scans with five repeated B-scans at each position), with a field-of-view of 1.1 mm × 1.1 mm centered on the optic nerve head (ONH). The total acquisition time for a single OCTA volume was approximately 50 seconds.

2.3. Resampled circumpapillary B-scan

Before measuring any retinal anatomical features, we resampled the 3-dimensional (3D) dataset in post-processing from 400 A-lines/B-scan to 512 A-lines/B-scan to create square *en face* images. The five repeated B-scans at each location were aligned and averaged so that each dataset consisted of 512 B-scans only. We then obtained resampled circumpapillary B-scans centered on the ONH, with radii approximately 300 μm–550 μm. An 11 pixel-thick ring (~23 μm) with a radius ~300–550 μm centered on the ONH was plotted, and A-lines located along the ring were sorted as a function of angle (also see Fig. 2).

2.4. Vis-OCT direct and resampled circumpapillary B-scan averaging

We performed both direct and resampled circumpapillary B-scan averaging for performance comparison. For direct B-scan averaging, we averaged nine consecutive B-scans (corresponding to 19 μm in physical space) using an established image registration algorithm (Guizar-Sicairos et al., 2008) between B-scans. For resampled circumpapillary B-scan averaging, we averaged nine adjacent A-lines from a resampled circumpapillary scan after sorting the A-lines as a function of angle.

2.5. Metrics to evaluate vis-OCT image quality

We used coefficient of variation (CV), acutance, and intralayer contrast to quantify vis-OCT image quality. CV is defined as

$$CV = \sigma/\mu, \quad (1)$$

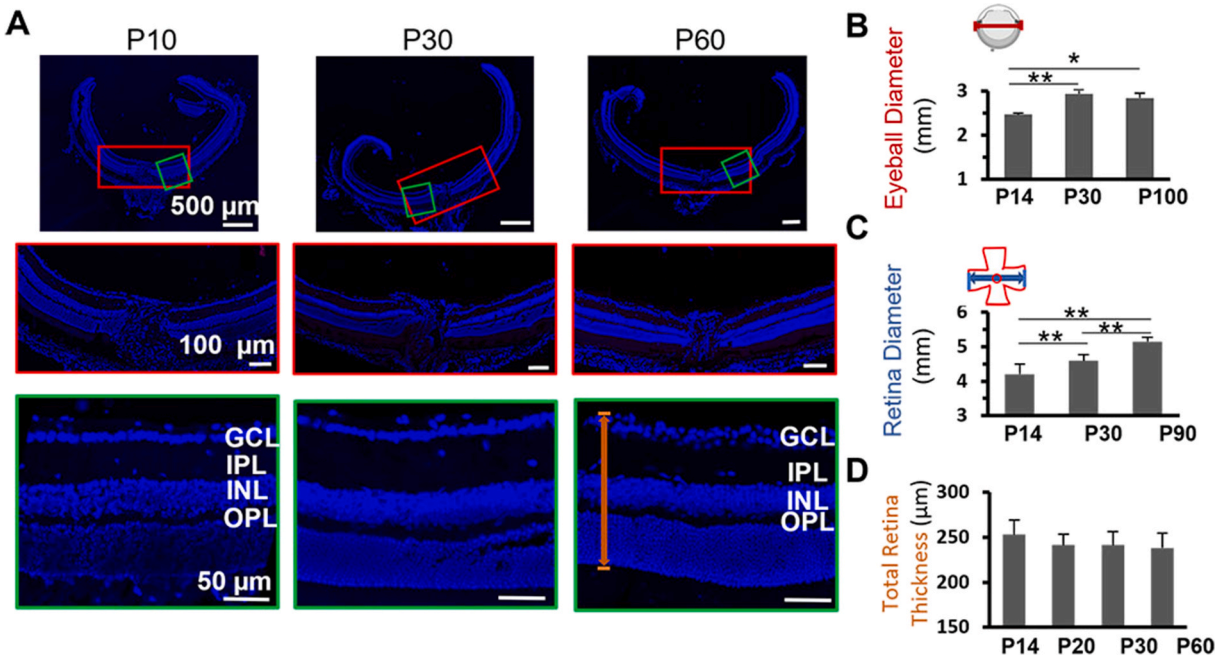

Fig. 1. The retina undergoes dynamic changes as the animal continues to grow during postnatal development. (A) Confocal microscopy images of retinal sections at P10, P30, and P60 immunostained by DAPI for nuclei. GCL: ganglion cell layer; IPL: inner plexiform layer; INL: inner nuclear layer; OPL: outer plexiform layer; (B) Eyeball diameter change; (C) Flat-mount retina diameter change; (D) Total retina thickness change. *: $P < 0.05$ and **: $P < 0.01$.

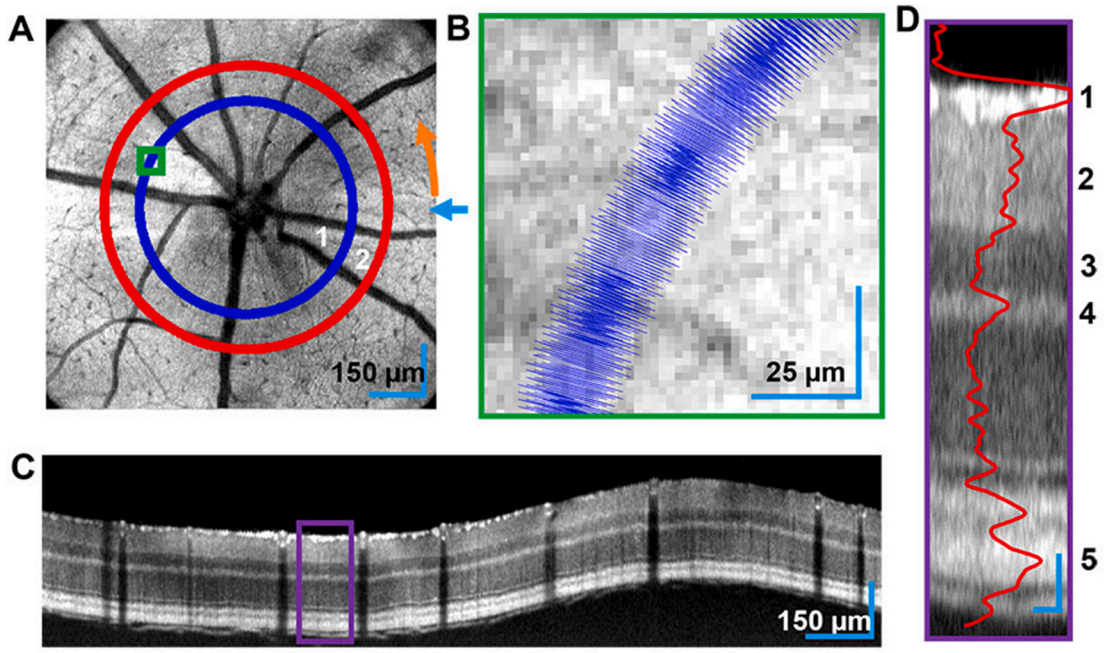

Fig. 2. Resampled circumpapillary averaging. (A) Example *en face* image. The rings highlight resampling paths. (B) Magnified view of the resampling path enclosed by the green box on ring 1 in panel A; (C) Resampled circumpapillary averaged B-scan imaged along the path highlighted by ring 2 in panel A; (D) Magnified view of the inner retina of the area highlighted by the purple box in panel C with overlaid resampled averaged A-line from the center of panel D shown in red. Scale bar: 50 μm. (For interpretation of the references to colour in this figure legend, the reader is referred to the Web version of this article.)

where σ is the standard deviation of the selected retinal layer and μ is the mean of the selected retinal layer. A lower CV corresponds with the lower variation of intensity values within the retinal layer, indicating a less noisy layer. Acutance (Choong et al.; Miller et al., 2020) is defined as

$$Acutance = \frac{1}{N}\sum_{x_i}\sum_{y_i}\sqrt{G_x^2 + G_y^2}, \quad (2)$$

where N is the total number of pixels in the image; x_i is the horizontal pixel index; y_i is the vertical pixel index; G_x is the horizontal image gradient; and G_y is the vertical image gradient. Acutance is a measure of image sharpness, with sharper images associated with a higher acutance. Image defocus and shadows from the hyaloid can reduce acutance. Intralayer contrast (Girard et al., 2011) is defined as

$$Intralayer\ \ contrast = \left|\frac{I_S - I_N}{I_S + I_N}\right|, \quad (3)$$

where I_S is the mean intensity in a region of interest of a retinal layer situated directly beneath a hyaloid shadow and I_N is the mean intensity of a region of interest from the same retinal layer as and directly adjacent to I_S but free from the hyaloid shadow. Intralayer contrast provides a quantitative measure of the effect from the hyaloid shadow. The intralayer contrast varies between 0 and 1, where a value closer to 0 corresponds to a lesser impact from the hyaloid.

2.6. Immunostaining and confocal microscopy

After acquiring vis-OCT data, we euthanized the mice with Euthasol (15.6 mg/mL; Virbac, Greely, CO, USA) and perfused them with 4% paraformaldehyde (PFA) in phosphate-buffered saline. Eyes were dissected and prepared for cryo-sectioning (Feng et al., 2013; Miller et al., 2020). Eyecups were embedded in Tissue-Tek Optimal Cutting Temperature (O.C.T.) medium (Fisher Scientific). We immunolabeled tissue sections of 20-μm thickness with the ONH as a landmark. The antibodies include anti-Tuj1 preconjugated with Alexa Fluor-488 (1:1000; BioLegend, San Diego, CA) and 4′, 6-diamidino-2-phenylindole (DAPI, VECTASHIELD®, Vector Laboratories). Confocal images were performed using a Zeiss LSM 800 microscope (Carl Zeiss AG, Oberkochen, Germany). Images of whole retinal cups were captured using 10x tile scans, while images of ONHs were captured with 20x z-stacks (Miller et al., 2020).

2.7. Manual retinal layer thickness measurements

We used ImageJ (Schneider et al., 2012) to measure the retinal layer thickness: the retinal nerve fiber layer (RNFL)/ganglion cell layer (GCL), the inner plexiform layer (IPL), the inner nuclear layer (INL), and the total retinal thickness (TRT, which included from the RNFL to the retinal pigment epithelium, RPE). We performed 24 measurements per resampled circumpapillary B-scan or confocal image, where all measurements were taken approximately 300–550 μm from the ONH. Mean and standard deviation were calculated for each mouse, and pooled standard deviation was calculated for each age group. All standard deviations reported and shown in plots are pooled standard deviations. Statistically significant differences between measurements are defined by having p values of less than 0.05 in one-way ANOVA with post-hoc Tukey test.

3. Results

3.1. Retinas undergo dynamic changes as the animal continues to grow during postnatal development

We quantified the eyeball size, the flat-mount retina diameter, and the TRT at different postnatal ages (Fig. 1A). As the animal continues to grow, the eyeball diameter increased 18.6% from 2.47 ± 0.03 mm (n = 14) at P14 to 2.93 ± 0.12 mm (n = 12) at P30 ($P < 0.01$, One-way ANOVA with post-hoc Tukey test; same statistics test was applied below, Fig. 1B). The eyeball size remained stable at P100 (2.84 ± 0.03 mm, n = 14, p = 0.78, Fig. 1B). At the same time, the retina is also expanding (Fig. 1C). We measured the diameters of the flat-mount retinas and found the diameter increased from 4.20 ± 0.30 mm at P14 (n = 9) to 4.59 ± 0.20 mm at P30 (n = 8, $P < 0.01$) to 5.15 ± 0.12 mm at P90

(n = 6, P < 0.01, Fig. 1C). We further examined the overall retinal morphology at P10, P30, and P60 (Fig. 1A). The layer-specific structure was present at P10, right before eye-opening (Fig. 1A). Surprisingly, the TRT remained stable from 252.92 ± 12.73 μm at P14 (n = 5) to 241.19 ± 6.62 μm at P20 (n = 3) to 241.37 ± 6.04 μm at P30 (n = 3) to 238.00 ± 16.47 μm at P60 (n = 4, P = 0.32, One-way ANOVA, Fig. 1D). As the retinal circuits continue to mature after eye-opening, each sublayer may undergo different developmental changes. Next, we applied vis-OCT to examine the sublayer structural changes *in vivo* at different ages.

3.2. Resampled circumpapillary B-scan averaging improved inner retinal layer contrast compared with traditional B-scans for young mice

To improve inter-layer contrast in the retina, we introduced a resampled circumpapillary B-scan averaging technique (Fig. 2). Fig. 2A shows an *en face* image with two rings of radiuses 300 μm and 400 μm. The orange arrow indicates the direction of the path of the resampled B-scans. Fig. 2B is a magnified view of the area highlighted by the green box in Fig. 2A, showing part of the resampled path. A resampled circumpapillary B-scan is shown in Fig. 2C, corresponding to ring 2 in Fig. 2A. The blue arrow in both Fig. 2A indicates the location of the first A-line in Fig. 2C. Fig. 2D is a magnified view of the area highlighted by the purple box in Fig. 2C. An A-line taken from the middle of the magnified area is overlaid on in red. As shown in Fig. 2D, a clear peak in intensity on the A-line corresponds to (1) RNFL/GCL, immediately followed by a section of roughly uniform intensity corresponding to (2) IPL, a section of decreased intensity corresponding to (3) INL, and then the increased intensity of (4) outer plexiform layer (OPL). The peak in intensity corresponding to the OPL is vital in measuring the INL thickness, as it marks the lower boundary of the INL. Finally, the (5) RPE is a bright band at the bottom of the retina and is included in the TRT measurement. All these layer boundaries are clearly resolved in Fig. 2D, ensuring that manual measurements are reproducible.

Fig. 3 shows a side-by-side comparison of direct averaging and resampled circumpapillary averaging B-scan images for P14 and P60. We averaged all B-scans and A-lines nine times using these two methods. Fig. 3A shows direct averaging B-scan images with an amplitude-normalized A-line at the location highlighted in red on its corresponding B-scans to the left for P14 and P60. The key retinal layers which needed to be identified for the layer thickness measurements are labeled on the A-lines. Fig. 3A illustrates the difficulty in determining layer boundaries at key positions across the retina in the P14 age group from the direct averaging B-scan image. In particular, the boundaries between the IPL and INL and between the INL and OPL are not immediately identifiable. Fig. 3B shows the corresponding resampled circumpapillary averaging B-scans and A-lines. Compared with the direct averaging A-line, the resampled circumpapillary averaging A-line from the P14 group shows distinguished anatomical layers. For example, in the direct averaging A-line, the OPL corresponds to 2 discrete peaks with heights of 55% of the maximum OCT amplitude. In practice, this means that determining the onset of the OPL can be difficult when measuring the thickness of the INL. On the other hand, the OPL in the resampled circumpapillary averaging A-line corresponds to only one single peak, with a height of 66% of the maximum OCT amplitude, making thickness measurement less ambiguous. The B-scans and A-lines in the P60 group with both types of averaging are comparable. Fig. 3C and D compare the CV values for all retinal layers labeled in Fig. 3A and B. The CV values are very similar for layers in the P60 group between direct and resampled circumpapillary averaging methods. However, the resampled circumpapillary averaging method results in lower CV values for every layer measured in the P14 group.

3.3. Layer-specific changes of the developing mouse retina imaged by Vis-OCT

We imaged 6–9 healthy wild-type mice per age group to quantify the retinal layer structure *in vivo* by vis-OCT. Fig. 4A–D shows the *en face*, a non-averaged B-scan image, and a resampled circumpapillary B-scan

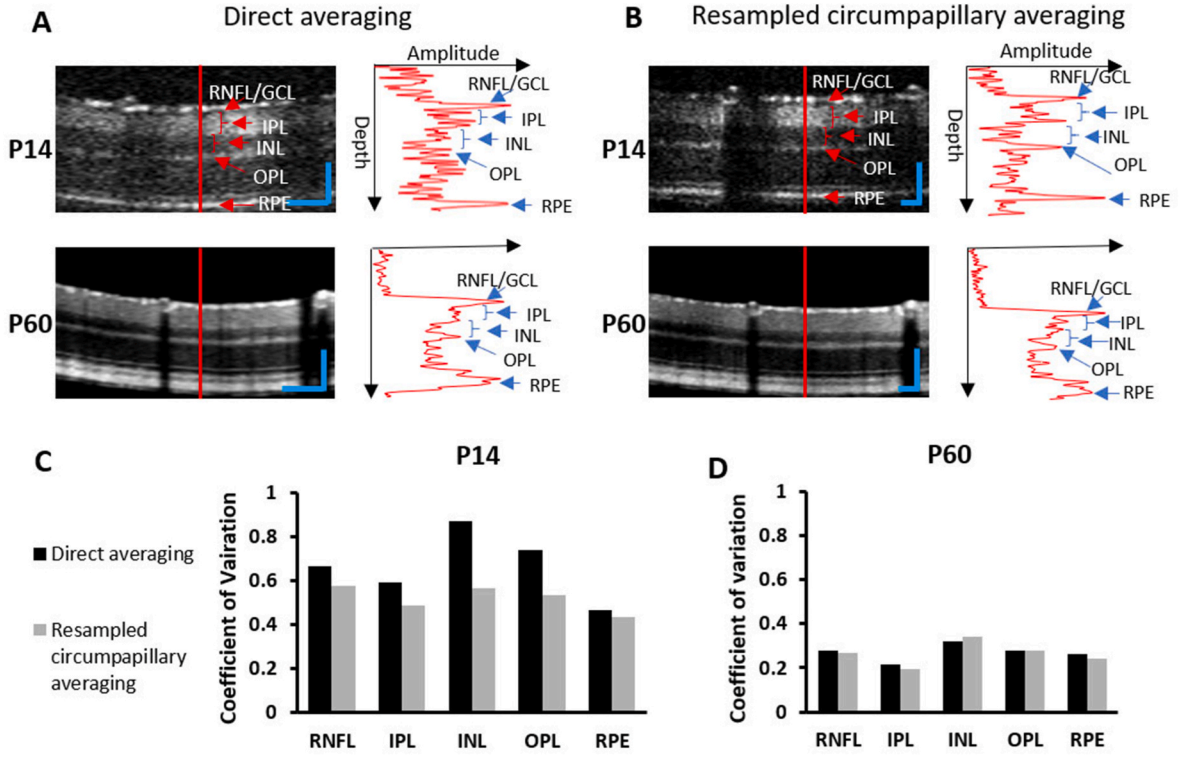

Fig. 3. Comparing retinal thickness measurements from direct and resampled circumpapillary averaging at P14 and P60. (A) B-scan images using direct averaging. Scale bar: 100 μm; (B) B-scan images using resampled circumpapillary averaging. Scale bar: 100 μm; (C) Comparing the coefficients of variation of retinal thickness measurements at P14; (D) Comparing the coefficients of variation of retinal thickness measurements at P60.

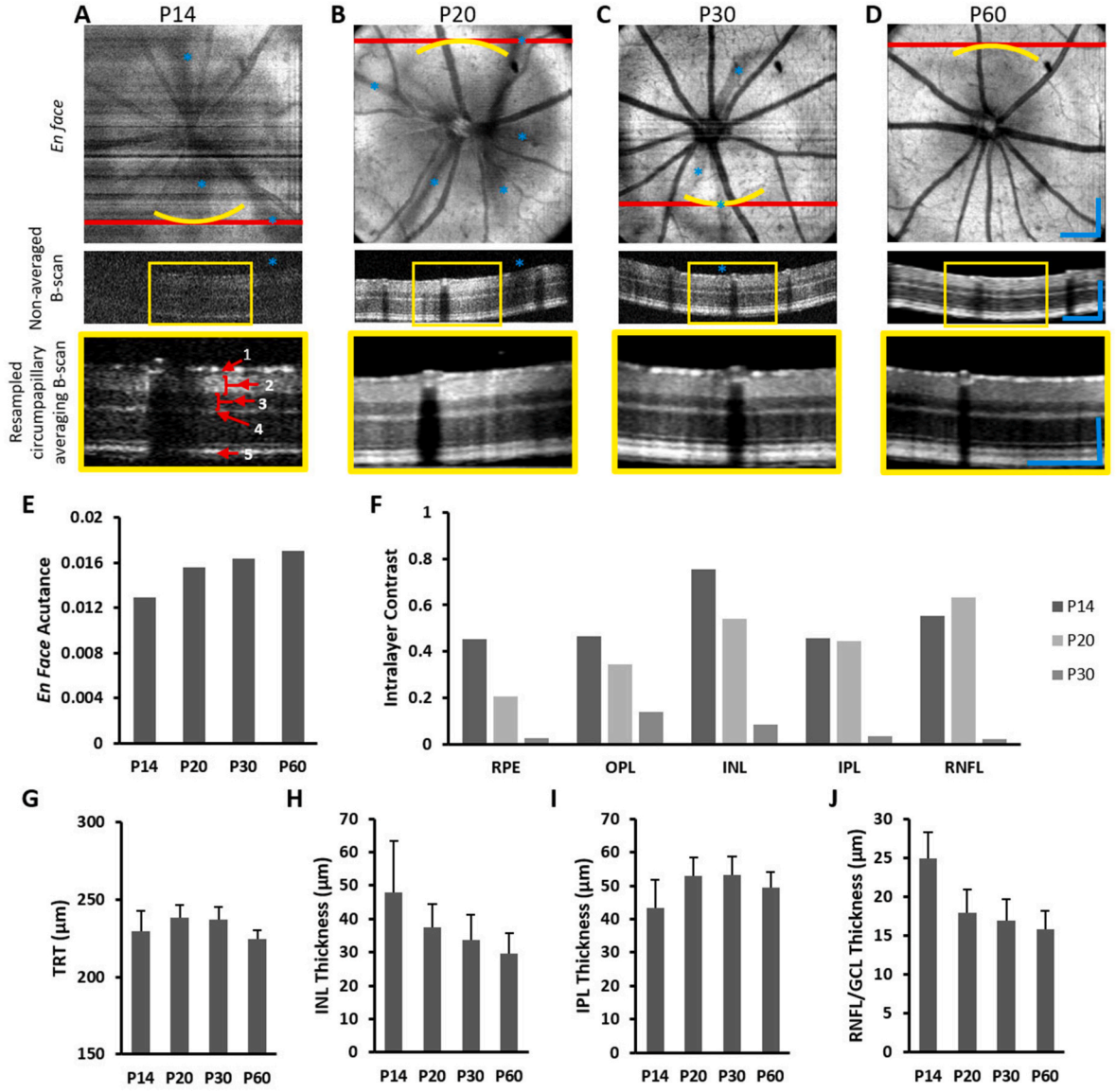

Fig. 4. Measured retinal layer thickness changes. (A–D) Representative vis-OCT *en face* images (top), non-averaged B-scan images (middle), and resampled circumpapillary averaged B-scan images (bottom) from P14, P20, P30, and P60. The red lines in the *en face* images highlight the location of the non-averaged B-scan images. The yellow curves in the *en face* images and the yellow boxes in the non-averaged B-scan images correspond to the locations of the resampled circumpapillary averaged B-scan images. Blue asterisks mark the location of hyaloid shadows. Scale bar: 200 µm; (E) En face acutance values from different age groups; (F) Intralayer contrast due to hyaloid shadows measured from the non-averaged B-scan images at different retinal layers from different age groups; (G–J) Measured TRT, INL, IPL, and RNFL/GCL thickness change with age from resampled circumpapillary averaged B-scan images. (For interpretation of the references to colour in this figure legend, the reader is referred to the Web version of this article.)

image for one mouse from each age group. The red lines on the *en face* images highlight the locations of the non-averaged B-scan images and the yellow curves on the *en face* images highlight the locations of the resampled circumpapillary averaging B-scan images. The yellow boxes on the non-averaged B-scan images correspond to the portions of the resampled circumpapillary averaging B-scan images. Blue asterisks indicate shadows from hyaloid vessels. For the P14 group (Fig. 4A), the *en face* and non-averaged B-scan images have poor signal quality due to the difficulty in focusing vis-OCT on the retina and attenuation from hyaloid vessels. Low signal intensity in the B-scan images can reduce the reliability of retinal thickness measurements taken directly from single, non-averaged B-scan images. For the P20 group (Fig. 4B), shadows cast by hyaloid vessels are still visible in the *en face* image and are highly attenuating on the B-scan image, but the overall *en face* and B-scan images show improved quality compared with those from the P14 group. For the P30 group (Fig. 4C), shadows cast by hyaloid vessels are still visible in the *en face* image but are not obvious on the B-scan image, no longer interfering with layer thickness measures across the entire retina. In the P60 mouse (Fig. 4D), there is no remaining evidence of hyaloid vessels.

A portion of each resampled circumpapillary averaging B-scan image is shown at the bottom of Fig. 4A–D. For each age group, regardless of how visible the inner retinal layer boundaries were in the non-averaged B-scans, each of the boundaries can be clearly distinguished in the resampled circumpapillary B-scan.

Fig. 4E plots the acutance value for each *en face* image shown in Fig. 4A–D. The acutance value increases with age, from 0.0129 at P14, to 0.0156 at P20, to 0.0164 at P30, and to 0.0171 at P60, which correlates with the decreasing shadows caused by hyaloid vessels over time. Fig. 4F shows the intralayer contrast values calculated from averaged B-scans at the corresponding locations highlighted in Fig. 4A–C. We selected the locations (highlighted by the blue asterisks) in the non-averaged B-scan

images, where hyaloid shadows are obvious from their corresponding *en face* images, to calculate the values of I_S and I_N according to Eq. (3). The same locations are also highlighted in the corresponding *en face* images together with the B-scan image locations. We calculated I_S from 5 adjacent A-lines centered at the asterisks and calculated I_N from 5 additional A-lines to the left. The intralayer contrast for P14 was uniformly high across all measured retinal layers, between 0.45 and 0.75, corresponding to high attenuation caused by the hyaloid vessels. At P20, intralayer contrast values are 0.34–0.64 for all measured retinal layers except the RPE, where intralayer contrast decreases to 0.21. By P30, intralayer contrast values are 0.14 or less for every measured retinal layer, corresponding to minimal effect from the hyaloid shadows.

We plotted the vis-OCT measurements for retinal layer thicknesses for each age group ($n = 6$ for P14, $n = 7$ for P20, $n = 9$ for P30, and $n = 9$ for P60; Fig. 4G–J). We found that the 3.3% increase in TRT was not significant from P14 (229.73 ± 10.29 μm) to P30 (237.33 ± 7.94 μm, $p = 0.27$, One-way ANOVA with post-hoc Tukey test; same statistics test was applied below), but the 5.5% decrease to 224.30 ± 5.83 μm at P60 ($p < 0.01$, Fig. 4G) was significant. Interestingly, we observed that the INL continuously decreased with age, from 45.40 ± 9.51 μm at P14, to 36.72 ± 6.60 μm at P20, to 33.73 ± 6.74 μm at P30, and 29.68 ± 6.05 μm at P60 ($p < 0.02$, Fig. 4H). The IPL thickness remained stable among all age groups (45.86 ± 7.47 μm at P14, 52.87 ± 5.50 μm at P20, 53.31 ± 5.33 μm at P30, 49.34 ± 4.89 μm at P60, $p = 0.07$, One-way ANOVA, Fig. 4I). The RNFL/GCL thickness also decreased with age, from 25.13 ± 3.78 μm at P14, to 17.91 ± 2.93 μm at P20, 16.87 ± 2.70 μm at P30, and 15.83 ± 2.53 μm ($p < 0.001$, Fig. 4J). Fig. 4 suggests that individual retinal layers undergo different developmental processes after eye-opening.

3.4. Vis-OCT and confocal measurements are highly correlated

We summarize the results of all retinal thickness measurements from *in vivo* vis-OCT and *ex vivo* confocal microscopy in Table 1, with the mean (±standard deviation) for the TRT, INL, IPL, and RNFL/GCL for each age group and compare them in Fig. 5. All vis-OCT thickness measurements were taken from resampled circumpapillary averaging B-scans. As a visual aid, Fig. 5A shows a typical direct averaged vis-OCT B-scan image from P60, and Fig. 5B shows a confocal microscopy image from P60. The central area of the cross-sections, between the two red vertical lines, was excluded to avoid any confounding effects of the ONH. The layers used in measurements are labeled in both the vis-OCT B-scan and the confocal microscopy image. We define a correlation constant between vis-OCT and confocal microscopy as the ratio between mean retinal layer thicknesses measured by vis-OCT and confocal microscopy. When the two measurements agree, the correlation constant is close to 1. Correlation constants consistently greater than or less than 1 would imply a bias where vis-OCT either over- or under-estimates the true measurement. Fig. 5C plots the correlation constants for all measured retinal layers. The correlation constant varies between 0.68 and 1.20 across the different retinal layers and age groups, and ranges from 0.90 to 1.20 across the retinal layers for the P14 age group. Fig. 5C shows that there is no consistent bias between vis-OCT and confocal measurements. We define the correlation coefficient between vis-OCT and confocal as Pearson's correlation coefficient (R^2) for a linear fit between the two measurements. We plotted each confocal retinal layer thickness measurement at each age group against the corresponding vis-OCT measurement (Fig. 5D). The R^2 is 0.995, and the slope of the best linear fit is 1.05. Together our data showed that vis-OCT and confocal measurements are highly correlated.

4. Discussion

We demonstrate vis-OCT's capability to visualize and track developmental changes in the retinal layer structure *in vivo*. Furthermore, we show that despite the limited image quality in the days around eye-opening, our resampled circumpapillary averaging technique enables repeatable inner retinal layer thickness measurements, which agree well with the measurements by confocal microscopy.

During early development, RGCs are amongst the first to differentiate before birth, followed by horizontal and amacrine cells, then rods and bipolar cells, and finally Müller cells (Cepko et al., 1996; Livesey and Cepko, 2001). Refinement of inner retinal layers continues as individual retinal neuron types mature during postnatal development, and this process is neuron-type-dependent and may require visual experience (Liu et al., 2007, 2009; Lucas and Schmidt, 2019; Maslim et al., 1986; Tian and Copenhagen, 2003). For example, intrinsically photosensitive RGC (ipRGC) dendrites broadly stratify within the correct layer early on, and each subtype undergoes dendritic refinement during the first postnatal month (Lucas and Schmidt, 2019). The M4 ipRGCs have dendrites stratifying closer to the GCL at P6 and then moving slightly closer to the middle of the IPL in adulthood, shaping the separation and formation of sublayers of the IPL (Lucas and Schmidt, 2019). After eye-opening, visual experience may play a role in modulating the dendritic refinement of RGCs in a type-dependent manner (Liu et al., 2007; Tian and Copenhagen, 2003) that also affects the IPL structure. Tracking the structural changes may offer new insights into the process of retina maturation.

One of the technical challenges in vis-OCT imaging is caused by the murine hyaloid vasculature system, which begins regressing after birth. This regression proceeds gradually and is considered mostly complete by P21 (Wang et al., 2019). However, we note the presence of shadows from hyaloid vessels still visible in 8 out of 9 mice at P30, is consistent with Kim et al., where hyaloid vessels were still visible in all mice at P28 (Kim et al., 2019). We found that the effect from the hyaloid vessels on vis-OCT retinal imaging diminishes over time from severe in P14 to minimal in P30, quantifying this effect with intralayer contrast, which decreased from an average of 0.54 at P14 to 0.06 at P30 (Fig. 4A–C, 4F). By P20, the overall image quality is largely unaffected by the presence and attenuation due to hyaloid vessels, corresponding to the 21% increase in *en face* acutance from P14 to P20 while the percent increase in *en face* acutance between P20 and P30 is only 5%, and between P30 and P60 is only 4% (Fig. 4E). However, heavy shadows cast on the B-scans at P20 still cause significant intralayer contrast and prevent the measurement of retinal layer thickness in those particular locations (Fig. 4B and F). We found that the resampled circumpapillary averaging B-scan improved contrast for mice at P14 (Fig. 3). The boundaries between the IPL and INL and between the INL and the OPL were particularly enhanced by resampled averaging. For older age groups, the inter-layer contrast using a traditional B-scan averaging technique was already sufficient, so the resampled circumpapillary B-scan did not significantly improve layer thickness measurements.

Table 1
List of retinal layer thicknesses measured by vis-OCT and confocal microscopy.

	TRT [μm]		INL [μm]		IPL [μm]		RNFL/GFL [μm]	
	Vis-OCT	Confocal	Vis-OCT	Confocal	Vis-OCT	Confocal	Vis-OCT	Confocal
P14	229.73 (10.29)	252.92 (17.38)	48.03 (9.51)	41.85 (10.53)	45.86 (7.47)	46.53 (7.28)	25.13 (3.78)	20.80 (3.66)
P20	238.13 (7.98)	241.19 (13.12)	37.57 (6.60)	34.82 (12.46)	52.87 (5.50)	47.45 (10.03)	17.91 (2.93)	19.38 (4.59)
P30	237.33 (7.94)	241.37 (17.59)	33.73 (6.74)	36.63 (11.29)	53.31 (5.33)	55.83 (8.34)	16.87 (2.69)	19.83 (4.32)
P60	224.30 (5.83)	238.00 (20.29)	29.76 (6.05)	39.22 (8.99)	49.34 (4.89)	45.50 (6.32)	15.83 (2.53)	23.18 (3.68)

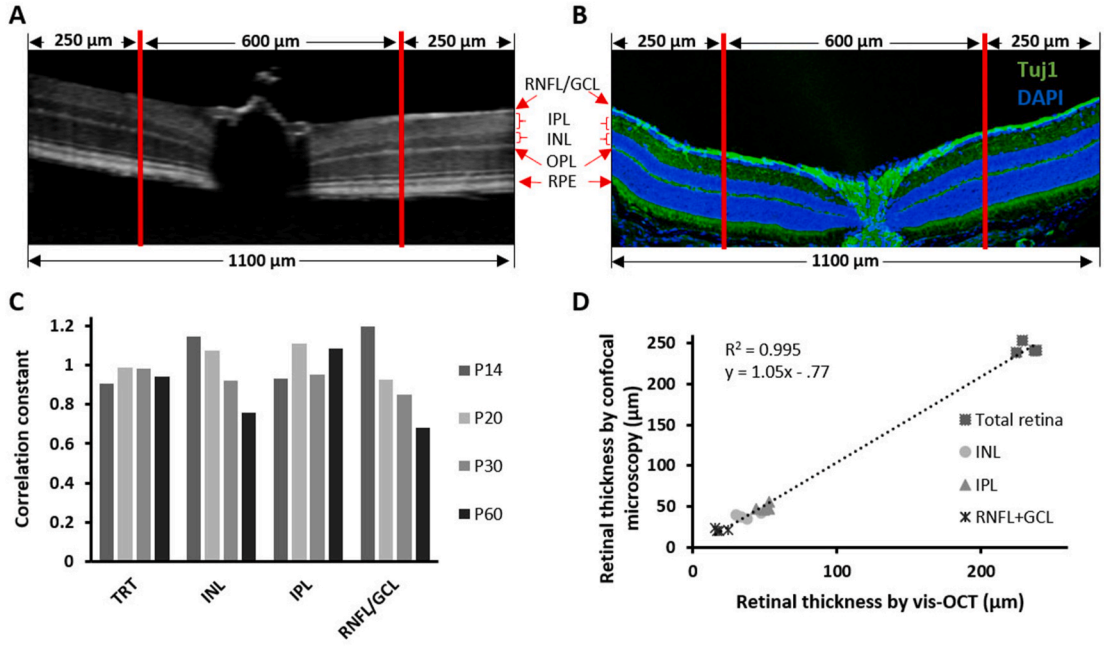

Fig. 5. Validating *in vivo* vis-OCT measurements with *ex vivo* confocal microscopy measurements. (A) *In vivo* vis-OCT direct averaged B-scan image from P60; (B) *Ex-vivo* confocal microscopy image from P60; (C) Correlation constant values between mean vis-OCT and mean confocal microscopy measurements of different retinal layers from different age groups. (D) Correlating vis-OCT and confocal microscopy measured retinal layer thicknesses.

We validated our vis-OCT findings by *ex vivo* confocal microscopy. We found that retinal layer thickness measured via vis-OCT and confocal microscopy agreed well with each other, even at P14. Specifically, the correlation constant between vis-OCT and confocal microscopy ranged from 0.68 to 1.2 across all measured retinal layers and age groups. This agrees with Ferguson et al., who reported a correlation constant between 0.70 and 1.17 amongst all the measured retinal layers in adult mice only (Ferguson et al., 2013). They reported a mean correlation constant for TRT of 0.96 while ours is 0.95. The range of our correlation constants at P14 is even smaller, from 0.90 to 1.20, implying a good agreement between vis-OCT and confocal microscopy layer measurements by the time of eye-opening. Additionally, we report a correlation coefficient of 0.995 when TRT is included, which agrees well with previously published correlation coefficient values ranging from 0.89 to 0.99 for layer thickness measurements in adult retinas (Cheng et al., 2018; Ferguson et al., 2013; Fischer et al., 2009; Xie et al., 2018).

Our study of the normal developmental changes in the murine retinal layer structure builds the foundation to track pathological structural alterations in diseased conditions. Vis-OCT has been applied to visualizing the RGC fiber bundles within a 0.8-mm region in wild-type rats (Pi et al., 2020) and sensing early RGC damages before detectable RNFL thinning in a nerve-crushed mouse model (Yi et al., 2016). Developmental eye disorders, such as retinopathy of prematurity, congenital glaucoma, and aniridia, may be relatively rare but have devastating consequences. These patients often suffer permanent vision loss at a very young age. Early detection of neural damage and assessing its progression can reduce the risk of further vision loss up to 50% (Davis et al., 2016; Gracitelli et al., 2015; Jonas et al., 2017; Welp et al., 2016). In other words, timely initiation of treatment can prevent ongoing neural damage and preserve vision long-term. However, detecting the disease at its earliest stages and monitoring disease progression continue to be substantial clinical challenges. Our study supports vis-OCT's potential to track changes in murine models of pediatric eye diseases for better understanding the retinal neurodegeneration and its underlying mechanisms, which may offer new tools for better diagnosis and treatment of eye diseases.

Funding

This work was supported in part by NIH grants R01EY026078, R01EY029121, R01EY028304, R01EY019949, and R01EY026286.

Commercial relationship disclosure

L. Beckmann, None; Z. Cai, None; J. Cole, None; D. A. Miller, None; M. Liu, None; M. Grannonico, None; X. Zhang, None; H. J. Ryu, None; P. A. Netland, None; X. Liu, None; H. F. Zhang, Opticent Health (I).

References

Beros, J., Rodger, J., Harvey, A.R., 2018. Developmental retinal ganglion cell death and retinotopicity of the murine retinocollicular projection. Dev. Neurobiol. 78, 51–60.
Cang, J., Savier, E., Barchini, J., Liu, X., 2018. Visual function, organization, and development of the mouse superior colliculus. Annu. Rev. Vis. Sci. 4, 239–262.
Cepko, C.L., Austin, C.P., Yang, X., Alexiades, M., Ezzeddine, D., 1996. Cell fate determination in the vertebrate retina. Proc. Natl. Acad. Sci. U.S.A. 93, 589–595.
Chen, S., Shu, X., Yi, J., Fawzi, A., Zhang, H.F., 2016. Dual-band optical coherence tomography using a single supercontinuum laser source. J. Biomed. Opt. 21, 66013-66013.
Cheng, J., Sohn, E.H., Jiao, C., Adler, K.L., Kaalberg, E.E., Russell, S.R., Mullins, R.F., Stone, E.M., Tucker, B.A., Han, I.C., 2018. Correlation of optical coherence tomography and retinal histology in normal and Pro23His retinal degeneration pig. Transl. Vis. Sci. & Technol. 7, 18-18.
Chong, S.P., Zhang, T., Kho, A., Bernucci, M.T., Dubra, A., Srinivasan, V.J., 2018. Ultrahigh resolution retinal imaging by visible light OCT with longitudinal achromatization. Biomed. Opt Express 9, 1477–1491.
Choong, Y.F., Rakebrandt F Fau - North, R.V., North Rv Fau - Morgan, J.E., Morgan, J.E., Acutance, an Objective Measure of Retinal Nerve Fibre Image Clarity..
Cole, J.D., Rodrigues, C., Norat, P., Gao, J., Provencio, I., Netland, P.A., Liu, X., 2021. Neural damage and neuroprotection with glaucoma development in aniridia. Curr. Neurobiol. 12, 14–19.
Davis, B.M., Crawley, L., Pahlitzsch, M., Javaid, F., Cordeiro, M.F., 2016. Glaucoma: the retina and beyond. Acta Neuropathol. 132, 807–826.
Feng, L., Zhao, Y., Yoshida, M., Chen, H., Yang, J.F., Kim, T.S., Cang, J., Troy, J.B., Liu, X., 2013. Sustained ocular hypertension induces dendritic degeneration of mouse retinal ganglion cells that depends on cell type and location. Investig. Ophthalmol. & Vis. Sci. 54, 1106–1117.
Ferguson, L.R., Dominguez Ii, J.M., Balaiya, S., Grover, S., Chalam, K.V., 2013. Retinal thickness normative data in wild-type mice using customized miniature SD-OCT. PloS One 8, e67265.
Fischer, M.D., Huber, G., Beck, S.C., Tanimoto, N., Muehlfriedel, R., Fahl, E., Grimm, C., Wenzel, A., Remé, C.E., van de Pavert, S.A., Wijnholds, J., Pacal, M., Bremner, R.,

Seeliger, M.W., 2009. Noninvasive, in vivo assessment of mouse retinal structure using optical coherence tomography. PloS One 4, e7507.
Ginsberg, J., Bove, K.E., Cuesta, M.G., 1980. Aplasia of the optic nerve with aniridia. Ann. Ophthalmol. 12, 433–439.
Girard, M.J.A., Strouthidis, N.G., Ethier, C.R., Mari, J.M., 2011. Shadow removal and contrast enhancement in optical coherence tomography images of the human optic nerve head. Investig. Ophthalmol. & Vis. Sci. 52, 7738–7748.
Gracitelli, C.P., Abe, R.Y., Tatham, A.J., Rosen, P.N., Zangwill, L.M., Boer, E.R., Weinreb, R.N., Medeiros, F.A., 2015. Association between progressive retinal nerve fiber layer loss and longitudinal change in quality of life in glaucoma. JAMA Ophthalmol. 133, 384–390.
Guizar-Sicairos, M., Thurman, S.T., Fienup, J.R., 2008. Efficient subpixel image registration algorithms. Opt. Lett. 33, 156–158.
Jonas, J.B., Aung, T., Bourne, R.R., Bron, A.M., Ritch, R., Panda-Jonas, S., 2017. Glaucoma. Lancet 390, 2183–2193.
Kim, T.-H., Son, T., Le, D., Yao, X., 2019. Longitudinal OCT and OCTA monitoring reveals accelerated regression of hyaloid vessels in retinal degeneration 10 (rd10) mice. Sci. Rep. 9, 16685-16685.
Kondo, H., 2018. Foveal hypoplasia and optical coherence tomographic imaging. Taiwan J. Ophthalmol. 8, 181–188.
Liu, X., Grishanin, R.N., Tolwani, R.J., Renteria, R.C., Xu, B., Reichardt, L.F., Copenhagen, D.R., 2007. Brain-derived neurotrophic factor and TrkB modulate visual experience-dependent refinement of neuronal pathways in retina. J. Neurosci. 27, 7256–7267.
Liu, X., Robinson, M.L., Schreiber, A.M., Wu, V., Lavail, M.M., Cang, J., Copenhagen, D. R., 2009. Regulation of neonatal development of retinal ganglion cell dendrites by neurotrophin-3 overexpression. J. Comp. Neurol. 514, 449–458.
Livesey, F.J., Cepko, C.L., 2001. Vertebrate neural cell-fate determination: lessons from the retina. Nat. Rev. Neurosci. 2, 109–118.
Lucas, J.A., Schmidt, T.M., 2019. Cellular properties of intrinsically photosensitive retinal ganglion cells during postnatal development. Neural Dev. 14, 8.
Maslim, J., Webster, M., Stone, J., 1986. Stages in the structural differentiation of retinal ganglion cells. J. Comp. Neurol. 254, 382–402.
McCulley, T.J., Mayer, K., Dahr, S.S., Simpson, J., Holland, E.J., 2005. Aniridia and optic nerve hypoplasia. Eye 19, 762–764.
Miller, D.A., Grannonico, M., Liu, M., Kuranov, R.V., Netland, P.A., Liu, X., Zhang, H.F., 2020. Visible-light optical coherence tomography fibergraphy for quantitative imaging of retinal ganglion cell axon bundles. Transl. Vis. Sci. Technol. 9, 11.
Netland, P.A., Scott, M.L., Boyle, J.W.t., Lauderdale, J.D., 2011. Ocular and systemic findings in a survey of aniridia subjects. J. AAPOS 15, 562–566.
Pi, S., Hormel, T.T., Wei, X., Cepurna, W., Morrison, J.C., Jia, Y., 2020. Imaging retinal structures at cellular-level resolution by visible-light optical coherence tomography. Opt. Lett. 45, 2107–2110.
Rubinoff, I., Beckmann, L., Wang, Y., Fawzi, A.A., Liu, X., Tauber, J., Jones, K., Ishikawa, H., Schuman, J.S., Kuranov, R., Zhang, H.F., 2019. Speckle reduction in visible-light optical coherence tomography using scan modulation. Neurophotonics 6, 041107.
Sanes, J.R., Masland, R.H., 2015. The types of retinal ganglion cells: current status and implications for neuronal classification. Annu. Rev. Neurosci. 38, 221–246.
Schneider, C.A., Rasband, W.S., Eliceiri, K.W., 2012. NIH Image to ImageJ: 25 years of image analysis. Nat. Methods 9, 671–675.
Sernagor, E., Eglen, S.J., Wong, R.O., 2001. Development of retinal ganglion cell structure and function. Prog. Retin. Eye Res. 20, 139–174.
Shu, X., Beckmann, L., Zhang, H., 2017. Visible-light optical coherence tomography: a review. J. Biomed. Opt. 22, 1–14.
Smith, A.M., Mancini, M.C., Nie, S., 2009. Bioimaging: second window for in vivo imaging. Nat. Nanotechnol. 4, 710–711.
Tian, N., Copenhagen, D.R., 2003. Visual stimulation is required for refinement of ON and OFF pathways in postnatal retina. Neuron 39, 85–96.
Wang, Z., Liu, C.-H., Huang, S., Chen, J., 2019. Assessment and characterization of hyaloid vessels in mice. J. Vis. Exp. 147, 10.3791/59222.
Welp, A., Woodbury, R.B., McCoy, M.A., Teutsch, S.M., 2016. Making Eye Health a Population Health Imperative. Vision for Tomorrow, Washington (DC).
Xie, W., Zhao, M., Tsai, S.-H., Burkes, W.L., Potts, L.B., Xu, W., Payne, H.R., Hein, T.W., Kuo, L., Rosa, R.H., 2018. Correlation of spectral domain optical coherence tomography with histology and electron microscopy in the porcine retina. Exp. Eye Res. 177, 181–190.
Yi, J., Puyang, Z., Feng, L., Duan, L., Liang, P., Backman, V., Liu, X., Zhang, H.F., 2016. Optical detection of early damage in retinal ganglion cells in a mouse model of partial optic nerve crush injury. Investig. Ophthalmol. & Vis. Sci. 57, 5665–5671.
Young, R.W., 1984. Cell death during differentiation of the retina in the mouse. J. Comp. Neurol. 229, 362–373.
Zhang, T., Kho, A.M., Srinivasan, V.J., 2019. Improving visible light OCT of the human retina with rapid spectral shaping and axial tracking. Biomed. Opt Express 10, 2918–2931.